

Spectral Analysis of Jet Substructure with Neural Network: Boosted Higgs Case

Sung Hak Lim^a, Mihoko M. Nojiri^{a,b,c}

^a*Theory Center, IPNS, KEK, Tsukuba, Ibaraki 305-0801, Japan*

^b*The Graduate University of Advanced Studies (Sokendai), Tsukuba, Ibaraki 305-0801, Japan*

^c*Kavli IPMU (WPI), University of Tokyo, Kashiwa, Chiba 277-8583, Japan*

E-mail: sunghak.lim@kek.jp, nojiri@post.kek.jp

ABSTRACT: Jets from boosted heavy particles have a typical angular scale which can be used to distinguish it from QCD jets. We introduce a machine learning strategy for jet substructure analysis using a spectral function on the angular scale. The angular spectrum allows us to scan energy deposits over the angle between a pair of particles in a highly visual way. We set up an artificial neural network (ANN) to find out characteristic shapes of the spectra of the jets from heavy particle decays. By taking the discrimination of Higgs jets from QCD jets as an example, we show that the ANN based on the angular spectrum has similar performance to existing taggers. In addition, some improvement is seen in the case that additional extra radiations occur. Notably, the new algorithm automatically combines the information of the multi-point correlations in the jet.

KEYWORDS: Standard Model, LHC, QCD, jet substructure, spectroscopy, artificial neural network

Contents

1	Introduction	2
2	A Spectral Function of Jet Substructure	3
3	Spectral Analysis with Artificial Neural Network	6
4	Discussion and Conclusion	11

1 Introduction

At multi TeV pp colliders such as the LHC, boosted heavy particles can be produced and form a single collimated cluster of particles. Such a localized cluster is distinguished from QCD jets from quarks or gluons by the substructures of the cluster [1]. For this purpose, consistent definitions of substructures of jets have been studied extensively. There are various methods for identifying the jet substructures, such as strategies based on cluster decomposition [1–8] and shape variables [9–13]. These methods focus on different features of jet substructures to maximize the discrimination power. For the case of Higgs, W, and Z boson decaying hadronically into two quarks, a critical feature is a two-prong substructure inside. Because the key features depend on nature of the parent particle of a jet, there are several frameworks that can be applied to jets [14–18].

In this paper, we propose a new framework to identify jet substructures using a spectral function similar to the angular structure function [14, 19, 20]. Spectral analysis is widely used technique to explore quantum worlds. A notable example of spectral analysis is proton nuclear magnetic resonance ($^1\text{H-NMR}$) spectroscopy of organic molecules. Organic molecules consist mostly of carbon skeleton and hydrogen atoms. Shift and splitting of the resonant frequency of the hydrogen depend on interactions between the hydrogen and the rest of the molecular substructure. Hence, a $^1\text{H-NMR}$ spectrum can be used to determine molecular structures as illustrated in Figure 1. We develop a suitable spectrum of jet substructures, so that spectral analysis techniques are applicable to identify the nature of a given jet.

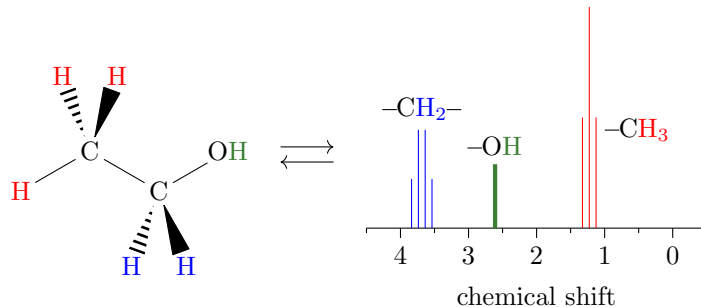


Figure 1. Molecular structure of ethanol and its $^1\text{H-NMR}$ spectrum. The intensity, location and splitting of peaks allow us to identify the original molecular structure. The chemical shift is the resonant frequency of hydrogen relative to a reference frequency.

An artificial neural network (ANN) is a useful technique for analyzing the spectrum. Jet substructure analyses based on ANN are gaining attention recently and have been studied in various contexts. The analyses are categorized mainly into two groups with different inputs. One group utilizes special-purpose observables and uses ANN to identify a correlation between substructures [15, 17, 21] similar to analyses with a boosted decision tree [22, 23]. The other group uses the jet constituents directly and uses ANN to find out particular substructures in a jet. This group is again categorized into two subgroups depending on how you interpret jet constituents. One can interpret jet constituents as an image [24] and use image recognition techniques [25–29]. The other strategies are to interpret a jet as a sequence of data, such as clustering sequence of the jet algorithms [30–35], and utilize ANN for sequential data analysis [36, 37]. Our approach is different from these approaches, namely our network is requested to analyze an event-by-event spectrum of a jet. This approach reduces the inputs of the ANN significantly but it can still learn characteristic non-local correlations in a jet from a heavy particle like the non-local neural networks for video classification [38]. We will show that our approach improves the separation between Higgs jets and QCD jets in natural manner.

This paper is organized as follows. In Sec. 2, we define the spectral function $S_2(R)$ and describe its nature. We also explain the setup of our Monte-Carlo simulations to show the performance. In Sec. 3, we introduce the spectral analysis with ANN and present a comparison of performance between ANN with $S_2(R)$ and ANN with previously known quantity D_2 [12] for two-prong substructures. Sec. 4 is devoted for summary and discussions.

2 A Spectral Function of Jet Substructure

Inspired by $^1\text{H-NMR}$, we introduce a spectral function of jet substructure. The perturbative description of jets is analogous to organic molecules. Partons from a heavy particle decay determine primary geometry of a jet, corresponding to a carbon skeleton which fixes the structure of the organic molecule. The final objects in the jet are hadronized particles from the partons, and we consider them analogous to the hydrogen atoms surrounding the carbon skeleton. We then use correlations between two jet constituents to define a spectrum from transverse momenta of all particle pairs i and j , $p_{T,i}$ and $p_{T,j}$, and their angular distance $R_{ij} = \sqrt{\eta_{ij}^2 + \phi_{ij}^2}$, where η_{ij} is pseudorapidity and ϕ_{ij} is azimuthal angle between i and j . The spectrum is better to be infrared and collinear (IRC) safe, namely invariant under soft and collinear radiations. If the IRC safety is not satisfied, then Kinoshita-Lee-Nauenberg theorem [39, 40] is not applicable, and such a spectral density is hard to be estimated from perturbative QCD calculations.

We define a binned spectral function for two-point correlation,

$$S_2(R; \Delta R) = \frac{1}{\Delta R} \sum_{\substack{i,j \in \text{jet} \\ R_{ij} \in [R, R+\Delta R)}} p_{T,i} p_{T,j}, \quad (2.1)$$

where ΔR is the bin width. In a continuum limit $\Delta R \rightarrow 0$,¹ this spectral function turns into,

$$S_2(R) = \int_{\vec{R}_i, \vec{R}_j \in \text{jet}} d\vec{R}_i d\vec{R}_j P_T(\vec{R}_i) P_T(\vec{R}_j) \cdot \delta(R - R_{ij}), \quad (2.2)$$

where $d\vec{R} P_T(\vec{R})$ is a p_T sum of constituents in a neighborhood $d\vec{R}$ of \vec{R} , and $\delta(x)$ is the Dirac δ function. The spectrum may be easily generalized into three-point or multi-point spectral functions, analogous to energy correlation functions [11] and energy flow polynomials [18].

¹For more formal description, see [41].

The $S_2(R)$ spectrum is IRC safe. A radiation $a(p_{T,a}) \rightarrow b(p_{T,b}) + c(p_{T,c})$ does not change $S_2(R)$ if b or c is soft because $p_{T,b}p_{T,c} \rightarrow 0$. A collinear splitting also does not change $S_2(R)$ because two momenta stay at the original $\vec{R} = (\eta, \phi)$ coordinate. Note that summing the autocorrelation term p_T^2 in Eq. 2.1 is necessary to achieve IRC safety at $R = 0$ because the crossing term $p_{T,b}p_{T,c}$ after splitting is originated from the autocorrelation term $p_{T,a}^2$.

The IRC safety of $S_2(R)$ is also understood in the context of C -correlators [18, 41]. The $S_2(R)$ is a special case of C -correlators with an unbounded non-smooth angular weighting function $f_2(\hat{p}_i, \hat{p}_j) = \delta(R - R_{ij})$. If we replace the Dirac δ function to a bounded smooth function, for example, $\delta(x) \rightarrow (|a|\sqrt{\pi})^{-1}e^{-(x/a)^2}$, then the Taylor expansion of $\delta(x)$ transforms $S_2(R)$ into a series of IRC safe energy flow polynomials [18] with two vertices. The series converges to $S_2(R)$ in the limit $a \rightarrow 0$, and the IRC safety of $S_2(R)$ is understood asymptotically.

The $S_2(R)$ spectrum is constrained by kinematics. The integrals of $S_2(R)$ are one-point and two-point energy correlation functions [11], which are approximately the transverse momentum $p_{T,\text{jet}}$ and the mass m_{jet} of the jet,

$$\int_0^\infty dR S_2(R) = \left(\sum_{i \in \text{jet}} p_{T,i} \right)^2 \approx p_{T,\text{jet}}^2, \quad (2.3)$$

$$\int_0^\infty dR R^2 S_2(R) = \sum_{i,j \in \text{jet}} p_{T,i} p_{T,j} R_{ij}^2 \approx 2m_{\text{jet}}^2. \quad (2.4)$$

These integrals imply the physical interpretations of $S_2(R)$. $S_2(R)$ measures contribution to $p_{T,\text{jet}}^2$ from pairs of jet constituents at a particular relative angle R , and $R^2 S_2(R)$ measures contribution to m_{jet}^2 from the pairs at the angle R .

We perform a Monte Carlo study of classifying Higgs jets and QCD jets using $S_2(R)$ spectrum. We generate $pp \rightarrow Zj$ events and $pp \rightarrow Zh$ events followed by $h \rightarrow b\bar{b}$, and use the leading jet of the events as training sample of one prong and two prong jets respectively. Each sample is generated at the leading order in QCD using `MadGraph5_aMC@NLO 2.6.1` [42] with parton distribution function (PDF) set `NNPDF 2.3 LO` at $\alpha_S(m_Z) = 0.130$ [43]. Z bosons are forced to decay into neutrinos so that they are invisible to the detector. The events are showered and hadronized by `Pythia 8.226` [44] with Monash tune [45]. We include effects of underlying events such as multi-parton interaction and beam remnant treatment but we do not take pile-ups into account.

Finally, we simulate detector response using `Delphes 3.3.3` [46] with their default ATLAS setup. Jets are reconstructed from calorimeter tower using anti- k_T algorithm [35] with a jet radius parameter $R_{\text{jet}} = 1.0$ implemented in `fastjet 3.3.0` [47, 48]. We study substructures of leading p_T jets having $p_{T,\text{jet}} \in [300, 400]$ GeV and $m_{\text{jet}} \in [100, 150]$. The characteristic angle between two b quarks from the boosted Higgs boson is then $R_{b\bar{b}} \gtrsim 2m_h/p_{T,\text{jet}} \approx 0.83$. Hence, the choice of the jet radius is enough to catch them efficiently. For Zh events, we additionally require that at least one b parton momentum in the matrix element level is located within $R \leq 1$ from the jet center to avoid contamination of hard initial state radiations. After these preselections, we have 256691 Zh and Zj events for training ANN. When we test ANN, we use a testing sample generated independently to the training sample.

We show typical pixelated jet images and $S_2(R; 0.1)$ spectra of a Higgs boson jet and a quark jet in Figure 2. For the boosted Higgs boson, the $S_2(R; 0.1)$ distribution has two prominent peaks at $R = 0$ and $R_{b\bar{b}}$ which correspond to autocorrelation and cross-correlation of two b partons,

$$\begin{aligned} p_T(\vec{R}) &= p_{T,b} \cdot \delta(\vec{R} - \vec{R}_b) + p_{T,\bar{b}} \cdot \delta(\vec{R} - \vec{R}_{\bar{b}}), \\ S_2(R) &= \left(p_{T,b}^2 + p_{T,\bar{b}}^2 \right) \cdot \delta(R) + 2p_{T,b}p_{T,\bar{b}} \cdot \delta(R - R_{b\bar{b}}). \end{aligned} \quad (2.5)$$

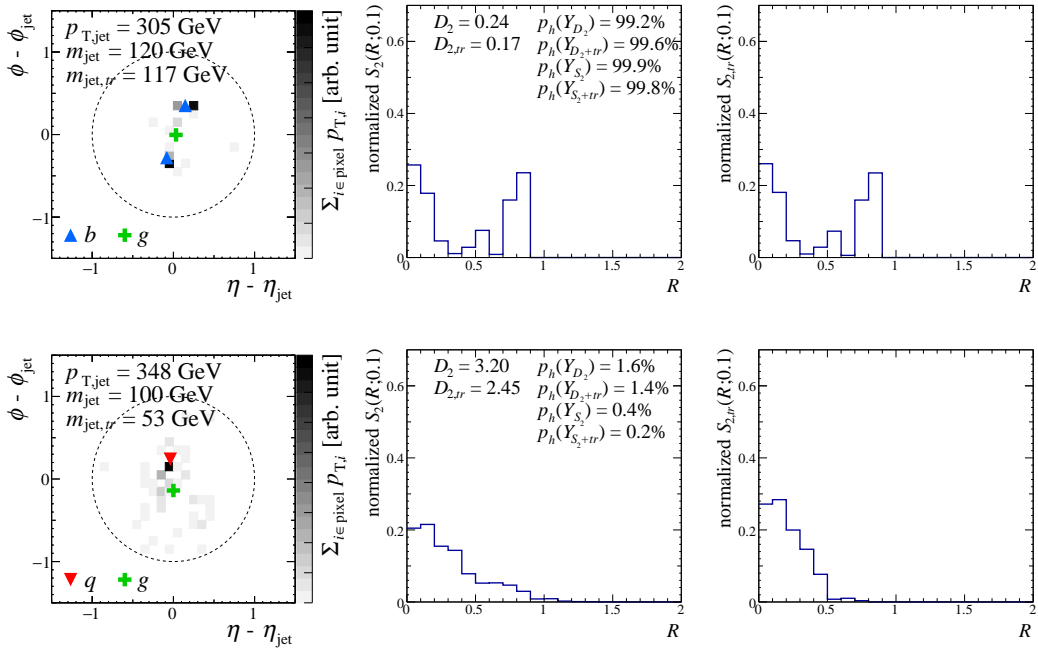


Figure 2. The pixelated jet image (left), two-point spectrum $S_2(R;0.1)$ (center), and the trimmed spectrum $S_2(R;0.1)$ (right) of a typical Higgs jet (top) and a typical quark jet (bottom). The sum of the bins of each spectrum is normalized to 1. The red reversed triangles, blue triangles, and green plus symbols in the pixelated jet images indicate direction of light quarks, b quarks and gluons obtained from the matrix element including order α_S radiations. We show the Higgs-like probability $p_h(Y_X)$ in an ANN model \mathcal{N}_X defined by Eq. 3.9.

Because the Higgs boson decays spherically, the two peaks typically have comparable intensities, $p_{T,b}^2 + p_{T,\bar{b}}^2 \simeq 2p_{T,b}p_{T,\bar{b}}$, as shown in Figure 2. After the initial parton production, parton shower starts. Each splitting of a parton is characterized by the angle between daughter partons and their momenta. $S_2(R)$ sums up those individual splittings. The peaks in R is smeared by the parton shower and hadronization, but it is not easy to modify the initial radiation pattern. Figure 2 (top center) is qualitatively similar to the $^1\text{H-NMR}$ spectrum in Figure 1. In Figure 2, we also show the quark jet spectrum. It does not have distinctive peaks. Instead, the spectrum have a gradually decreasing spectrum from $R = 0$ to high R .

Note that the $S_2(R)$ spectrum is not completely independent to the angular structure function $\Delta\mathcal{G}(R)$ in [14]. The function $\Delta\mathcal{G}(R)$ is related to $S_2(R)$ by

$$\mathcal{G}(R) = \frac{\int_0^R dR' R'^2 S_2(R')}{\int_0^\infty dR' R'^2 S_2(R')}, \quad (2.6)$$

$$\Delta\mathcal{G}(R) = \frac{d \log \mathcal{G}(R)}{d \log R} = \frac{R \cdot R^2 S_2(R)}{\int_0^R dR' R'^2 S_2(R')}. \quad (2.7)$$

This $\Delta\mathcal{G}(R)$ is a Higuchi's fractal dimension [49] of $\mathcal{G}(R)$ which measure irregularity of $\mathcal{G}(R)$ over R . QCD jets have a uniform $\Delta\mathcal{G}(R)$ distribution on average because of approximate scale invariance of QCD [14, 19, 20]. On the other hand, $\mathcal{G}(R)$ of the multi-prong jet shows sharp peaks at some angular scales [14]. In [14], a number of peaks and peak heights are used to classify jets. In this paper, we construct classifier using ANN from $S_2(R)$ spectrum to utilize the global structures of the jet.

3 Spectral Analysis with Artificial Neural Network

We now feed these event-by-event $S_2(R; \Delta R)$ spectra to our ANN to build a classifier between the boosted Higgs jet and the QCD jet. First, we prepared an equal number of Higgs jets and QCD jets to avoid overfitting from unbalanced data. We use `TFLearn` [50] with backend `TensorFlow` [51] for the ANN analysis. An input set we consider includes $S_2(R; 0.1)$ up to angular scale $R < 2$,

$$\{x_i\}_{S_2} = \{p_{T,\text{jet}}, m_{\text{jet}}, S_2(0; 0.1), \dots, S_2(1.9; 0.1)\}. \quad (3.1)$$

Note that $R = 2$ is the diameter of our jet definition. All the input data $\{x_i\}$ are standardized, i.e., $x_i \rightarrow (x_i - \bar{x}_i)/\sigma(x_i)$, where \bar{x}_i and $\sigma(x_i)$ are the mean and the standard deviation of x_i of the whole training sample including both Higgs jets and QCD jets. The network is configured with four hidden layers having (400, 300, 200, 100) ReLU nodes and an output layer with two softmax nodes giving a Higgs-like score y_{S_2} . To avoid overtraining, we insert dropout layers with rate 20% between each hidden layer. The network is trained by Adam optimizer [52] with learning rate 0.001, $\beta_1 = 0.99$ and $\beta_2 = 0.999$ minimizing a categorical cross-entropy,

$$\sum_i \begin{cases} -\log[y_{S_2}(\{x_i\})] & \text{Higgs jets,} \\ -\log[1 - y_{S_2}(\{x_i\})] & \text{QCD jets.} \end{cases} \quad (3.2)$$

We call this network as \mathcal{N}_{S_2} . In the trained network, Higgs jets have scores near 1, while QCD jets have scores near 0. We validate \mathcal{N}_{S_2} using the testing samples.

We compare the performance of \mathcal{N}_{S_2} with the performance of a network trained with special-purpose observables. First, we choose D_2 which is sensitive to the two-prong substructure of jets [12]. D_2 is defined by a ratio of two-point and three-point energy correlation functions e_2^β and e_3^β as follows.

$$e_2^\beta = \frac{1}{p_{T,\text{jet}}^2} \sum_{\substack{i,j \in \text{jet} \\ i < j}} p_{T,i} p_{T,j} R_{ij}^\beta, \quad (3.3)$$

$$e_3^\beta = \frac{1}{p_{T,\text{jet}}^3} \sum_{\substack{i,j,k \in \text{jet} \\ i < j < k}} p_{T,i} p_{T,j} p_{T,k} R_{ij}^\beta R_{jk}^\beta R_{ki}^\beta, \quad (3.4)$$

$$D_2^\beta = \frac{e_3^\beta}{(e_2^\beta)^3}, \quad (3.5)$$

where the summations of e_2^β and e_3^β run over all jet constituents. We use $\beta = 2$ for further discussion. For Higgs jets, D_2 tends to have a small value because e_3^β is suppressed by collinear and soft radiations while e_2^β is large because the pairs of jet constituents with $R_{ij} \sim R_{b\bar{b}}$ dominate. To optimize the performance of D_2 , we prepare another neural network which maps following inputs to the Higgs-like score y_{D_2} ,

$$\{x_i\}_{D_2} = \{p_{T,\text{jet}}, m_{\text{jet}}, D_2^{\beta=2}\}. \quad (3.6)$$

Again, the input data is normalized to $[0, 1]$, i.e., $x_i \rightarrow (x_i - \min x_i)/(\max x_i - \min x_i)$, where $\max x_i$ and $\min x_i$ are the maximum and the minimum of x_i in the training sample respectively. We use smaller hidden layers (100, 100) ReLU nodes because the number of inputs is smaller. The other ANN setups are identical to the $S_2(R)$ analysis. We call this network as \mathcal{N}_{D_2} .

To make ANN learn a hierarchy between soft and hard radiations, variables after jet trimming [53] are useful. To obtain trimmed quantities, we first reconstruct k_T subjets [31, 32] with $R_{\text{sub}} = 0.2$ from constituents of the jet and remove subjets having transverse momentum $p_{T,\text{subjet}} < f_{\text{cut}} \cdot p_{T,\text{jet}}$, where $f_{\text{cut}} = 0.05$. In the right panel of Figure 2, we show $S_{2,tr}(R)$ spectrum, which is $S_2(R)$

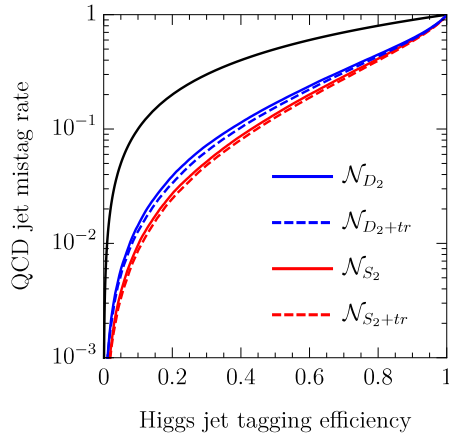


Figure 3. ROC curves of ANN classifiers for Higgs jets and QCD jets with inputs Eq. 3.1, Eq. 3.6, Eq. 3.7, and Eq. 3.8.

spectrum of the trimmed jet constituents, of a Higgs jet and a QCD jet. The $S_2(R)$ spectrum before trimming is shown in the central panel. The two-prong substructure of a Higgs jet is hard, and the double peak structure appears both in $S_2(R)$ and $S_{2,tr}(R)$. On the other hand, the spectrum of a QCD jet is significantly modified, which means that soft activities dominate the $S_2(R)$ spectrum. This shows a difference between $S_2(R)$ and $S_{2,tr}(R)$ contains useful information for the classification.

We then prepare two networks \mathcal{N}_{D_2+tr} and \mathcal{N}_{S_2+tr} taking inputs $\{x_i\}_{D_2+tr}$ and $\{x_i\}_{S_2+tr}$,

$$\{x_i\}_{D_2+tr} = \{x_i\}_{D_2} \cup \{p_{T,\text{jet},tr}, m_{\text{jet},tr}, D_{2,tr}^{\beta=2}\}, \quad (3.7)$$

$$\{x_i\}_{S_2+tr} = \{x_i\}_{S_2} \cup \{p_{T,\text{jet},tr}, m_{\text{jet},tr}, S_{2,tr}(0.0; 0.1), \dots, S_{2,tr}(1.9; 0.1)\}, \quad (3.8)$$

where the variables calculated after trimming have subscript tr . The other ANN setups are the same as the networks without trimmed variables, \mathcal{N}_{D_2} and \mathcal{N}_{S_2} . The networks \mathcal{N}_{D_2+tr} and \mathcal{N}_{S_2+tr} give us Higgs-like scores y_{S_2+tr} and y_{D_2+tr} .

We show receiver operating characteristic (ROC) curves of our ANN analyses \mathcal{N}_{D_2+tr} , \mathcal{N}_{D_2} , \mathcal{N}_{S_2} , and \mathcal{N}_{S_2+tr} in Figure 3. The ROC curves show that ANN with $S_2(R; \Delta R)$ rejects more QCD jets for fixed Higgs jet efficiency. At the Higgs tagging efficiency 0.4 (0.2), QCD jet mistag rate of \mathcal{N}_{S_2+tr} is reduced by 21.6% (26.7%) compared to that of \mathcal{N}_{D_2+tr} . This is expected because \mathcal{N}_{S_2+tr} uses two-point energy correlation from $S_2(R; \Delta R)$ and infers three-point energy correlation from correlations between different angular scales. For example, $S_2(R; \Delta R)$ of a three-prong jet having angular scales R_1 , R_2 , and R_3 has three peaks away from $R = 0$. The intensity of each peak gives a three-point energy correlation function, $e_3^\beta \approx p_{T,\text{jet}}^{-1} \cdot \sqrt{(\Delta R)^3 S_2(R_1; \Delta R) S_2(R_2; \Delta R) S_2(R_3; \Delta R) R_1^\beta R_2^\beta R_3^\beta}$. This results in better discrimination power. Also, adding trimmed observables allows ANN to learn hard and soft substructures separately. Hence, the ANN solve degeneracy in the variables before trimming and reject QCD jets better.

The network \mathcal{N}_{D_2+tr} uses minimum and simplest inputs; therefore it is easy to check ANN reaction to the input parameters m_{jet} , $p_{T,\text{jet}}$, and D_2 . We show distributions of the events in the Higgs-like probability $p_h(Y_{D_2+tr})$ and one of the inputs $\{x_i\}_{D_2+tr}$ plane in Figure 4. The Higgs-like probability of \mathcal{N}_X , $p_h(Y_X)$, is defined by probability to get a score y_X less than Y_X for the Higgs jet samples,

$$p_h(Y_X) = \Pr(y_X < Y_X | \text{Higgs jets}), \quad (3.9)$$

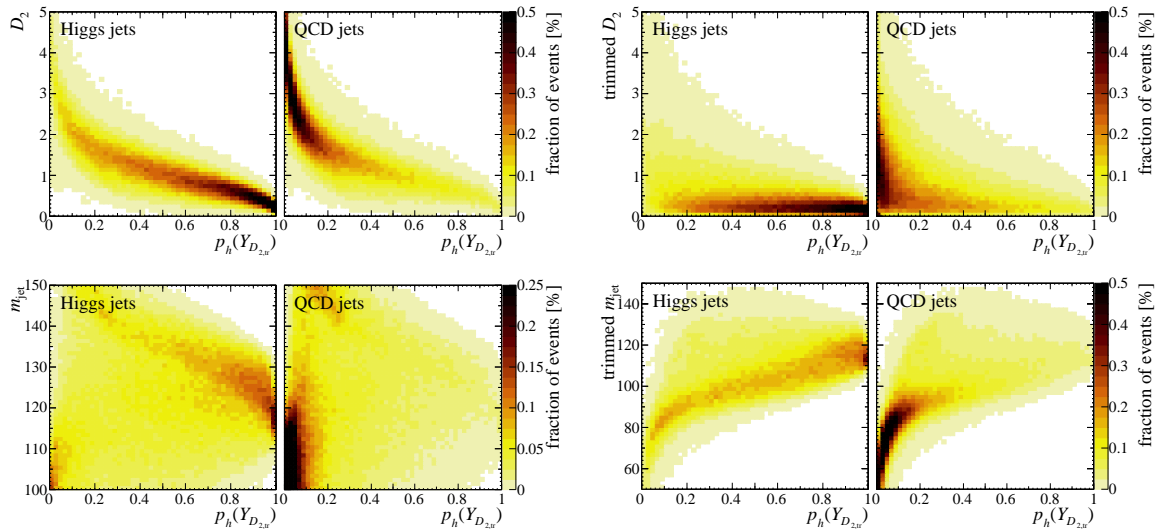


Figure 4. The distributions of Higgs jets and QCD jets in the Higgs-like probability $p_h(Y_{D_2+tr})$ and inputs in $\{x_i\}_{D_2+tr}$. For each pair of figures, the left is the distribution of Higgs jets and the right is the distribution of QCD jets.

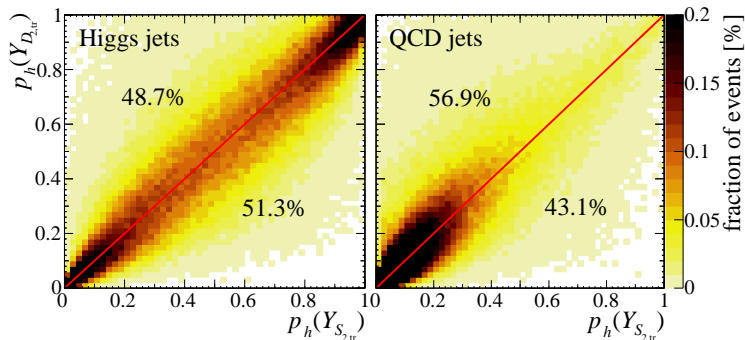


Figure 5. The distribution of Higgs-like probability in $p_h(Y_{S_2+tr})$ and $p_h(Y_{D_2+tr})$. The numbers in upper left and lower right area represent the fraction of events in the area.

where $\Pr(C|H)$ represents a conditional probability of C given H . A large $p_h(Y_X)$ means that the given jet is more Higgs-like in \mathcal{N}_X . Figure 4 shows that \mathcal{N}_{D_2+tr} tries to select jets having m_{jet} around 125 GeV up to energy loss, and small D_2 for capturing two-prong jets. Note that the \mathcal{N}_{D_2+tr} is trained by the QCD jets and the jets from a boosted Higgs boson with $m_H = 125$ GeV. Higgs jets with m_{jet} (trimmed m_{jet}) bigger (smaller) than $m_h = 125$ GeV are likely to be categorized as QCD jets. These shifts of the mass from the input Higgs mass are due to contamination of other activities, or large angle radiations from b jets. The distributions of QCD jets in Figure 4 show more clearly the definition of Higgs-like events. QCD jets with high $p_h(Y_{D_2+tr})$ have small $D_{2,tr}$, $m_{\text{jet},tr} \sim 115$ GeV, and $m_{\text{jet}} \sim 125$ GeV. The events with $m_{\text{jet}} \sim 130$ GeV and $p_h(Y_{D_2+tr}) < 0.2$ and events with $m_{\text{jet},tr} > 100$ GeV and $p_h(Y_{D_2+tr}) < 0.3$ are clearly reduced and instead distributing in higher $p_h(Y_{D_2+tr})$ region. Here \mathcal{N}_{D_2+tr} rejects QCD jets in a similar fashion that a cut based approach rejects QCD events.

We compare the Higgs-like probabilities in \mathcal{N}_{D_2+tr} and \mathcal{N}_{S_2+tr} in Figure 5 to see the origin

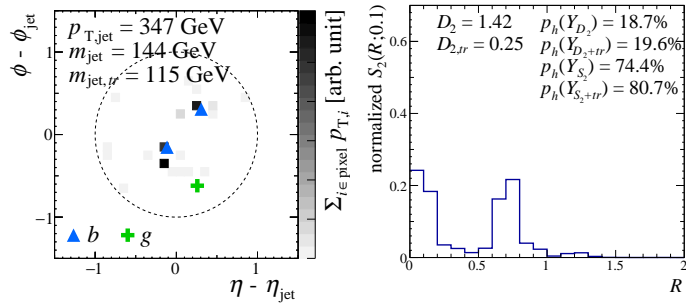


Figure 6. The pixelated jet image (left), and two-point spectrum $S_2(R; 0.1)$ (right) of a Higgs jet. The event is Higgs-like in the neural networks with $S_2(R)$, \mathcal{N}_{S_2} and \mathcal{N}_{S_2+tr} , but it is not in those with D_2 , \mathcal{N}_{D_2} and \mathcal{N}_{D_2+tr} . The sum of the bins of the spectrum is normalized to 1. The blue triangles and green plus symbols in the pixelated jet images indicate direction of b quarks and gluons obtained from the matrix element including order α_S radiations. We show the Higgs-like probability $p_h(Y_X)$ in an ANN model \mathcal{N}_X defined by Eq. 3.9.

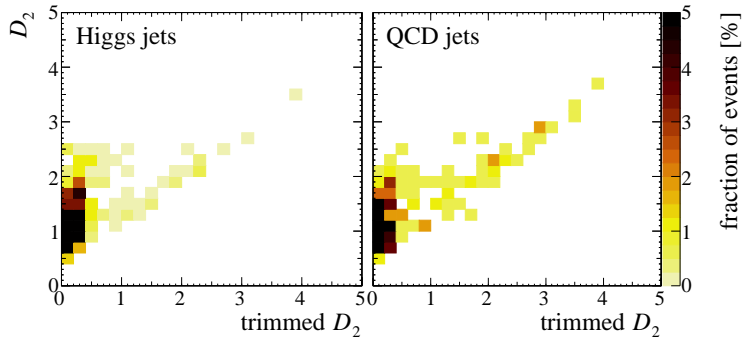


Figure 7. Distributions of Higgs jets (left) and QCD jets (right) in D_2 and $D_{2,tr}$, classified as Higgs jets in \mathcal{N}_{S_2+tr} but QCD jets in \mathcal{N}_{D_2+tr} . We particularly selects events having Higgs-like probabilities $p_h(Y_{D_2,tr}) < 30\%$ and $p_h(Y_{S_2,tr}) > 70\%$.

of improvement. The events are widely spreading around the line $p_h(Y_{D_2+tr}) = p_h(Y_{S_2+tr})$, which means that those two analyses have different selection criteria. To quantify the residual anticorrelation of \mathcal{N}_{D_2+tr} and \mathcal{N}_{S_2+tr} , we show the fractions of the events in the upper triangular region $p_h(Y_{D_2+tr}) > p_h(Y_{S_2+tr})$ and the lower triangular region $p_h(Y_{D_2+tr}) < p_h(Y_{S_2+tr})$. For Higgs jets, the lower triangular region contains more events compared with the upper triangular region, 51.3% of the total events. For QCD jets, the lower triangular region contains less events, 43.1%. Hence, \mathcal{N}_{S_2+tr} improves signal and background ratio S/B from \mathcal{N}_{D_2+tr} .

To figure out how \mathcal{N}_{S_2+tr} accepts more Higgs jets while rejecting more QCD jets compared to \mathcal{N}_{D_2+tr} , we will show three examples of the events located at off-diagonal regions in Figure 5. We show a Higgs jet in Figure 6, which is Higgs-like in \mathcal{N}_{S_2+tr} but regarded as a QCD jet in \mathcal{N}_{D_2+tr} , $p_h(Y_{D_2+tr}) = 19.6\%$ and $p_h(Y_{S_2+tr}) = 80.7\%$. This jet has a moderate wide-angle radiation on top of two-prong substructure which increases D_2 significantly. Remind that a Higgs jet originates from a color singlet particle while a QCD jet originates from a colored parton. Such wide-angle radiation is easily generated from a colored parton compared to a color singlet particle. \mathcal{N}_{D_2+tr} is distracted by a large D_2 and assigns this jet as a QCD jet even though the jet has small trimmed D_2 . \mathcal{N}_{S_2+tr} must have determined the jet as Higgs-like from the information of microscopic radiation patterns

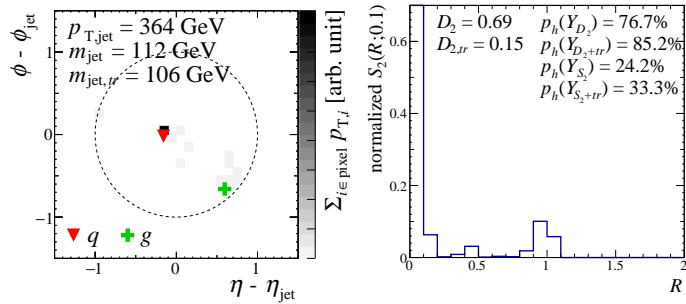


Figure 8. The Pixelated jet image (left), and two-point spectrum $S_2(R; 0.1)$ (right) of a Higgs jet. The event is Higgs-like in the neural networks with D_2 , \mathcal{N}_{D_2} and \mathcal{N}_{D_2+tr} , but it is not in those with $S_2(R)$, \mathcal{N}_{S_2} and \mathcal{N}_{S_2+tr} . The sum of the bins of the spectrum is normalized to 1. The red triangles and green plus symbols in the pixelated jet images indicate direction of light quarks and gluons obtained from the matrix element including order α_S radiations. We show the Higgs-like probability $p_h(Y_X)$ in an ANN model \mathcal{N}_X defined by Eq. 3.9.

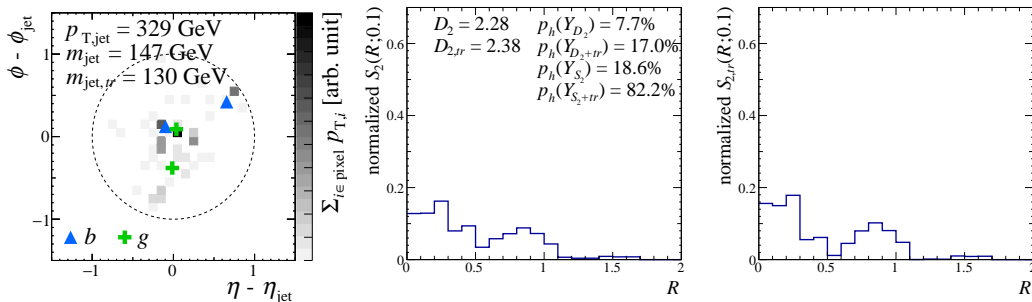


Figure 9. The Pixelated jet image (left), two-point spectrum $S_2(R; 0.1)$ (center), and trimmed spectrum $S_{2,tr}(R; 0.1)$ (right) of a Higgs jet which is Higgs-like only in the \mathcal{N}_{S_2+tr} . The sum of the bins of each spectrum is normalized to 1. The blue triangles and green plus symbols in the pixelated jet images indicate direction of b quarks and gluons obtained from the matrix element including order α_S radiations. We show the Higgs-like probability $p_h(Y_X)$ in an ANN model \mathcal{N}_X defined by Eq. 3.9.

in $S_2(R)$ which shows a clear double peak structure. Figure 7 shows D_2 and $D_{2,tr}$ distributions in events having $p_h(Y_{D_{2,tr}}) < 30\%$ and $p_h(Y_{S_{2,tr}}) > 70\%$. We can see that some, but not all, events with large D_2 but small $D_{2,tr}$ fall into this region.

The second example in Figure 8 is an event classified as a Higgs jet in \mathcal{N}_{D_2+tr} but categorized as a QCD jet in \mathcal{N}_{S_2+tr} . This jet has evident two-prong substructure, and hence, \mathcal{N}_{D_2+tr} classifies this jet as a Higgs jet. However, the two subjets are asymmetric in p_T . Such events appear frequently in QCD jet samples. We did not give subjet momenta to \mathcal{N}_{D_2+tr} , and the ANN classify the jet as a Higgs jet. In contrast, $S_2(R)$ knows the p_T asymmetry by comparing the peak intensity; see Eq. 2.5. Hence, \mathcal{N}_{S_2+tr} avoids these p_T asymmetric events populated by QCD jets while \mathcal{N}_{D_2+tr} finds the cut on the subjet p_T from the training samples. In the mass-drop tagger [1], the events with asymmetric p_T subjets are removed by hand.

The third example in Figure 9 is the case where only \mathcal{N}_{S_2+tr} , which takes into account of trimmed $S_2(R)$, classifies the jet as a Higgs jet. This jet has a two-prong substructure but deeply buried in radiations compared to Figure 8. As a result, D_2 is large, and $S_2(R)$ is similar to QCD jet with falling $S_2(R)$ structure toward high angular scale R . Trimming helps \mathcal{N}_{S_2+tr} this time

because \mathcal{N}_{S_2+tr} recognize hard and soft substructure separately by comparing $S_2(R)$ and $S_{2,tr}(R)$. Trimming does not alter the tail of $S_2(R)$ distribution, which means the structure at large R is hard. This should be compare with $S_2(R)$ and $S_{2,tr}(R)$ of typical QCD jets in Figure 2.

4 Discussion and Conclusion

In this paper, we have introduced a spectral analysis of jet substructure with the artificial neural network (ANN). Unlike the other ANN approach, our algorithm use the spectral function $S_2(R)$ constructed from p_T and R of the pair of particles in the jet. The $S_2(R)$ spectrum is useful in describing substructures with large angular separation by relatively small inputs. ANN can learn non-local correlations in jets from the spectrum. To show this, we have constructed ANN from $S_2(R)$, \mathcal{N}_{S_2} , and compare it with ANN from D_2 , \mathcal{N}_{D_2} . We have shown that \mathcal{N}_{S_2} discriminates between boosted Higgs jets and QCD jets with better performance compared to \mathcal{N}_{D_2} . Introducing trimming to $S_2(R)$ further helps to separate hard and soft substructures, and the ANN with trimmed observable outperforms the ANN without trimming. The improvement comes from the better handling of the cases with radiation from b parton or with contamination of other hadronic activities.

The improvement we observe is not large, because D_2 catches the two-prong substructure of the Higgs jet efficiently, but ANN analysis with $S_2(R)$ has much wider application. One of the merits of \mathcal{N}_{S_2} and \mathcal{N}_{S_2+tr} is that the analyses automatically take care of radiations from the b jet. Note that the existence of radiation has to be taken care of even in the original mass drop tagger by [1]. The $S_2(R)$ has information on three-point correlation and higher simultaneously and additional selections are not required. Consequently, $S_2(R)$ can be used in a cascade decay of a heavy particle, especially the top quark. We also note that $S_2(R)$ is sensitive to the color of the boosted heavy particle. We will show in a separate publication that a modified \mathcal{N}_{S_2} discriminate color octet resonance and color singlet resonance efficiently [54].

Acknowledgments

The authors would like to thank Amit Chakraborty and Tilman Plehn for useful discussions. This work was supported by the Grant-in-Aid for Scientific Research on Scientific Research B (No.16H03991, 17H02878 [MMN]) and Innovative Areas (16H06492 [MMN]), and by World Premier International Research Center Initiative (WPI Initiative), MEXT, Japan. The work of SHL was supported in part by MEXT KAKENHI Grant Number JP16K21730.

References

- [1] J. M. Butterworth, A. R. Davison, M. Rubin and G. P. Salam, *Jet substructure as a new Higgs search channel at the LHC*, *Phys. Rev. Lett.* **100** (2008) 242001, [[0802.2470](#)].
- [2] J. Thaler and L.-T. Wang, *Strategies to Identify Boosted Tops*, *JHEP* **07** (2008) 092, [[0806.0023](#)].
- [3] D. E. Kaplan, K. Rehermann, M. D. Schwartz and B. Tweedie, *Top Tagging: A Method for Identifying Boosted Hadronically Decaying Top Quarks*, *Phys. Rev. Lett.* **101** (2008) 142001, [[0806.0848](#)].
- [4] T. Plehn, G. P. Salam and M. Spannowsky, *Fat Jets for a Light Higgs*, *Phys. Rev. Lett.* **104** (2010) 111801, [[0910.5472](#)].
- [5] T. Plehn, M. Spannowsky, M. Takeuchi and D. Zerwas, *Stop Reconstruction with Tagged Tops*, *JHEP* **10** (2010) 078, [[1006.2833](#)].
- [6] D. E. Soper and M. Spannowsky, *Finding physics signals with shower deconstruction*, *Phys. Rev.* **D84** (2011) 074002, [[1102.3480](#)].

- [7] M. Dasgupta, A. Fregoso, S. Marzani and G. P. Salam, *Towards an understanding of jet substructure*, *JHEP* **09** (2013) 029, [[1307.0007](#)].
- [8] A. J. Larkoski, S. Marzani, G. Soyez and J. Thaler, *Soft Drop*, *JHEP* **05** (2014) 146, [[1402.2657](#)].
- [9] J. Thaler and K. Van Tilburg, *Identifying Boosted Objects with N -subjettiness*, *JHEP* **03** (2011) 015, [[1011.2268](#)].
- [10] Y.-T. Chien, *Telescoping jets: Probing hadronic event structure with multiple R 's*, *Phys. Rev.* **D90** (2014) 054008, [[1304.5240](#)].
- [11] A. J. Larkoski, G. P. Salam and J. Thaler, *Energy Correlation Functions for Jet Substructure*, *JHEP* **06** (2013) 108, [[1305.0007](#)].
- [12] A. J. Larkoski, I. Moult and D. Neill, *Power Counting to Better Jet Observables*, *JHEP* **12** (2014) 009, [[1409.6298](#)].
- [13] I. Moult, L. Necib and J. Thaler, *New Angles on Energy Correlation Functions*, *JHEP* **12** (2016) 153, [[1609.07483](#)].
- [14] M. Jankowiak and A. J. Larkoski, *Jet Substructure Without Trees*, *JHEP* **06** (2011) 057, [[1104.1646](#)].
- [15] K. Datta and A. Larkoski, *How Much Information is in a Jet?*, *JHEP* **06** (2017) 073, [[1704.08249](#)].
- [16] A. Chakraborty, A. M. Iyer and T. S. Roy, *A Framework for Finding Anomalous Objects at the LHC*, *Nucl. Phys.* **B932** (2018) 439–470, [[1707.07084](#)].
- [17] J. A. Aguilar-Saavedra, J. H. Collins and R. K. Mishra, *A generic anti-QCD jet tagger*, *JHEP* **11** (2017) 163, [[1709.01087](#)].
- [18] P. T. Komiske, E. M. Metodiev and J. Thaler, *Energy flow polynomials: A complete linear basis for jet substructure*, *JHEP* **04** (2018) 013, [[1712.07124](#)].
- [19] M. Jankowiak and A. J. Larkoski, *Angular Scaling in Jets*, *JHEP* **04** (2012) 039, [[1201.2688](#)].
- [20] A. J. Larkoski, *QCD Analysis of the Scale-Invariance of Jets*, *Phys. Rev.* **D86** (2012) 054004, [[1207.1437](#)].
- [21] K. Datta and A. J. Larkoski, *Novel Jet Observables from Machine Learning*, *JHEP* **03** (2018) 086, [[1710.01305](#)].
- [22] B. Bhattacharjee, S. Mukhopadhyay, M. M. Nojiri, Y. Sakaki and B. R. Webber, *Quark-gluon discrimination in the search for gluino pair production at the LHC*, *JHEP* **01** (2017) 044, [[1609.08781](#)].
- [23] Y.-T. Chien, A. Emerman, S.-C. Hsu, S. Meehan and Z. Montague, *Telescoping jet substructure*, [1711.11041](#).
- [24] J. Cogan, M. Kagan, E. Strauss and A. Schwartzman, *Jet-Images: Computer Vision Inspired Techniques for Jet Tagging*, *JHEP* **02** (2015) 118, [[1407.5675](#)].
- [25] L. G. Almeida, M. Backović, M. Cliche, S. J. Lee and M. Perelstein, *Playing Tag with ANN: Boosted Top Identification with Pattern Recognition*, *JHEP* **07** (2015) 086, [[1501.05968](#)].
- [26] L. de Oliveira, M. Kagan, L. Mackey, B. Nachman and A. Schwartzman, *Jet-images — deep learning edition*, *JHEP* **07** (2016) 069, [[1511.05190](#)].
- [27] P. Baldi, K. Bauer, C. Eng, P. Sadowski and D. Whiteson, *Jet Substructure Classification in High-Energy Physics with Deep Neural Networks*, *Phys. Rev.* **D93** (2016) 094034, [[1603.09349](#)].
- [28] P. T. Komiske, E. M. Metodiev and M. D. Schwartz, *Deep learning in color: towards automated quark/gluon jet discrimination*, *JHEP* **01** (2017) 110, [[1612.01551](#)].
- [29] G. Kasieczka, T. Plehn, M. Russell and T. Schell, *Deep-learning Top Taggers or The End of QCD?*, *JHEP* **05** (2017) 006, [[1701.08784](#)].

- [30] JADE collaboration, W. Bartel et al., *Experimental Studies on Multi-Jet Production in e^+e^- Annihilation at PETRA Energies*, *Z. Phys.* **C33** (1986) 23.
- [31] S. Catani, Y. L. Dokshitzer, M. H. Seymour and B. R. Webber, *Longitudinally invariant K_t clustering algorithms for hadron hadron collisions*, *Nucl. Phys.* **B406** (1993) 187–224.
- [32] S. D. Ellis and D. E. Soper, *Successive combination jet algorithm for hadron collisions*, *Phys. Rev.* **D48** (1993) 3160–3166, [[hep-ph/9305266](#)].
- [33] Y. L. Dokshitzer, G. D. Leder, S. Moretti and B. R. Webber, *Better jet clustering algorithms*, *JHEP* **08** (1997) 001, [[hep-ph/9707323](#)].
- [34] M. Wobisch and T. Wengler, *Hadronization corrections to jet cross-sections in deep inelastic scattering*, in *Monte Carlo generators for HERA physics. Proceedings, Workshop, Hamburg, Germany, 1998-1999*, 1998. [hep-ph/9907280](#).
- [35] M. Cacciari, G. P. Salam and G. Soyez, *The Anti- $k(t)$ jet clustering algorithm*, *JHEP* **04** (2008) 063, [[0802.1189](#)].
- [36] G. Louppe, K. Cho, C. Becot and K. Cranmer, *QCD-Aware Recursive Neural Networks for Jet Physics*, [1702.00748](#).
- [37] S. Egan, W. Fedorko, A. Lister, J. Pearkes and C. Gay, *Long Short-Term Memory (LSTM) networks with jet constituents for boosted top tagging at the LHC*, [1711.09059](#).
- [38] X. Wang, R. Girshick, A. Gupta and K. He, *Non-local neural networks*, *CVPR* (2018) , [[1711.07971](#)].
- [39] T. Kinoshita, *Mass singularities of Feynman amplitudes*, *J. Math. Phys.* **3** (1962) 650–677.
- [40] T. D. Lee and M. Nauenberg, *Degenerate Systems and Mass Singularities*, *Phys. Rev.* **133** (1964) B1549–B1562.
- [41] F. V. Tkachov, *Measuring multi - jet structure of hadronic energy flow or What is a jet?*, *Int. J. Mod. Phys.* **A12** (1997) 5411–5529, [[hep-ph/9601308](#)].
- [42] J. Alwall, R. Frederix, S. Frixione, V. Hirschi, F. Maltoni, O. Mattelaer et al., *The automated computation of tree-level and next-to-leading order differential cross sections, and their matching to parton shower simulations*, *JHEP* **07** (2014) 079, [[1405.0301](#)].
- [43] R. D. Ball et al., *Parton distributions with LHC data*, *Nucl. Phys.* **B867** (2013) 244–289, [[1207.1303](#)].
- [44] T. Sjöstrand, S. Ask, J. R. Christiansen, R. Corke, N. Desai, P. Ilten et al., *An Introduction to PYTHIA 8.2*, *Comput. Phys. Commun.* **191** (2015) 159–177, [[1410.3012](#)].
- [45] P. Skands, S. Carrazza and J. Rojo, *Tuning PYTHIA 8.1: the Monash 2013 Tune*, *Eur. Phys. J.* **C74** (2014) 3024, [[1404.5630](#)].
- [46] DELPHES 3 collaboration, J. de Favereau, C. Delaere, P. Demin, A. Giammanco, V. Lemaître, A. Mertens et al., *DELPHES 3, A modular framework for fast simulation of a generic collider experiment*, *JHEP* **02** (2014) 057, [[1307.6346](#)].
- [47] M. Cacciari, G. P. Salam and G. Soyez, *FastJet User Manual*, *Eur. Phys. J.* **C72** (2012) 1896, [[1111.6097](#)].
- [48] M. Cacciari and G. P. Salam, *Dispelling the N^3 myth for the k_t jet-finder*, *Phys. Lett.* **B641** (2006) 57–61, [[hep-ph/0512210](#)].
- [49] T. Higuchi, *Approach to an irregular time series on the basis of the fractal theory*, *Physica D: Nonlinear Phenomena* **31** (1988) 277 – 283.
- [50] A. Damien, “TFLearn: Deep learning library featuring a higher-level API for TensorFlow.” <http://tflearn.org/>.
- [51] “TensorFlow.” <https://www.tensorflow.org/>.

- [52] D. P. Kingma and J. Ba, *Adam: A method for stochastic optimization*, in *The 3rd International Conference for Learning Representations*, 2014. [1412.6980](#).
- [53] D. Krohn, J. Thaler and L.-T. Wang, *Jet Trimming*, *JHEP* **02** (2010) 084, [[0912.1342](#)].
- [54] A. Chakraborty, S. H. Lim and M. M. Nojiri, “Work in Progress.”